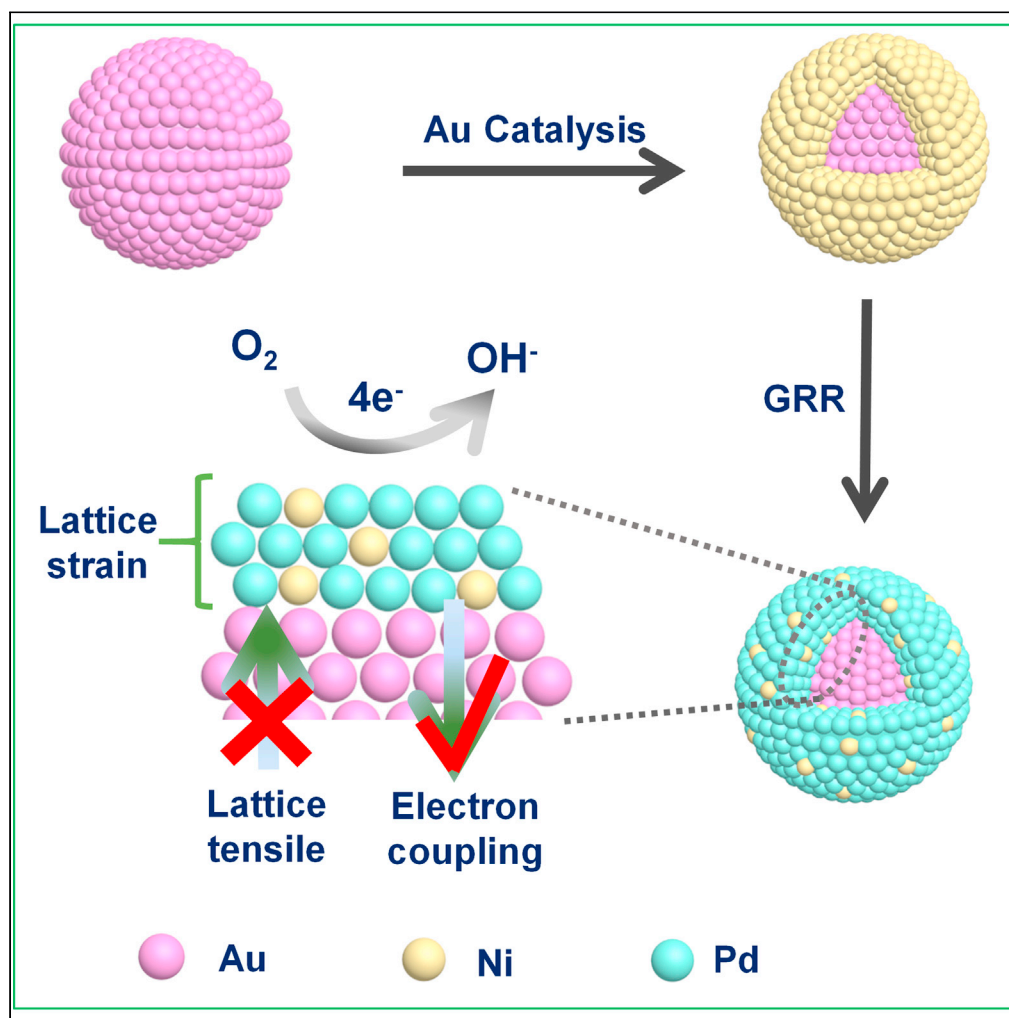**Article**

Electronic and lattice strain dual tailoring for boosting Pd electrocatalysis in oxygen reduction reaction

Qing Zeng, Danye Liu, Hui Liu, ..., Lin Xu, Xiang Wu, Jun Yang

chendong@ipe.ac.cn (D.C.)
xulin001@njnu.edu.cn (L.X.)
jyang@ipe.ac.cn (J.Y.)

Highlights

Electronic and lattice strain dual tailoring for boosting ORR activity of Pd metal

Dual tailoring achieves via a core-shell construction with sub-nano alloy shells

The optimized core-shell Au@NiPd particles display superior alkaline ORR behavior

Electrochemical evaluations and DFT calculations confirm the superior ORR activity

Article

Electronic and lattice strain dual tailoring for boosting Pd electrocatalysis in oxygen reduction reaction

Qing Zeng,[1,2] Danye Liu,[1,2] Hui Liu,[1,3] Penglei Cui,[1] Chaoquan Hu,[1,3] Dong Chen,[1,3,*] Lin Xu,[4,*] Xiang Wu,[5] and Jun Yang[1,2,3,6,*]

SUMMARY

Deliberately optimizing the d-band position of an active component *via* electronic and lattice strain tuning is an effective way to boost its catalytic performance. We herein demonstrate this concept by constructing core-shell Au@NiPd nanoparticles with NiPd alloy shells of only three atomic layers through combining an Au catalysis with the galvanic replacement reaction. The Au core with larger electronegativity modulates the Pd electronic configuration, while the Ni atoms alloyed in the ultrathin shells neutralize the lattice stretching in Pd shells exerted by Au cores, equipping the active Pd metal with a favorable d-band position for electrochemical oxygen reduction reaction in an alkaline medium, for which core-shell Au@NiPd nanoparticles with a Ni/Pd atomic ratio of 3/7 exhibit a half-wave potential of 0.92 V, specific activity of 3.7 mA cm^{-2}, and mass activity of 0.65 A mg^{-1} at 0.9 V, much better than most of the recently reported Pd-even Pt-based electrocatalysts.

INTRODUCTION

Oxygen reduction reaction (ORR), a crucial reaction in fuel cells and metal-air batteries for directly converting chemical energy into electricity energy (Bu et al., 2016; Chen et al., 2019a; Shao et al., 2019; Tao et al., 2020; Wang et al., 2011, 2018a, 2018b), has been considered as the rate-limiting step in these electrochemical devices. Robust and highly efficient electrocatalysts are therefore required to boost the sluggish kinetics of ORR (Chen et al., 2017, 2019b; Lu et al., 2017; Shao et al., 2019; Wang et al., 2018a, 2018b, 2019a; Ye et al., 2019). To this end, a wide variety of electrocatalysts has been continuously engineered and constructed, in which platinum (Pt)-based nanomaterials are dominant and serve as the most efficient catalysts for ORR owing to their unique electron structure for the fast reaction kinetics (Chen et al., 2019b; Kakati et al., 2014; Li et al., 2016; Wang et al., 2018a, 2018b, 2019b). Besides, palladium (Pd)-based nanomaterials are also regarded as the potential electrocatalysts for ORR, owing to similar physical properties to Pt, such as phase structure, atomic size, and electron configuration, which have been extensively studied, and their electrocatalytic performance for ORR is continuously improved (Antolini, 2009; Bu et al., 2018; Chen et al., 2016; Deming et al., 2015; Fu et al., 2014; Guo et al., 2014; Jiang et al., 2015, 2020; Koenigsmann et al., 2012; Koenigsmann and Wong, 2011; Lu et al., 2020; Li and Prakash, 2009; Liu et al., 2014, 2018; Noha and Shim, 2016; Neergat et al., 2011; Shao et al., 2006; Shim et al., 2011; Sonika et al., 2019; Xu et al., 2013; Yang et al., 2016, 2019).

Many studies have documented that the Pd shells grown on an Au core usually show excellent electrocatalytic properties for ORR, even beyond Pt in an alkaline medium owing to the electron transfer from Pd to Au that has relatively larger electronegativity (Chen et al., 2016; Fu et al., 2014; Noha and Shim, 2016; Sonika et al., 2019; Yang et al., 2016). This electronic coupling lowers the adsorption energy of oxygenated intermediates, e.g., O/OH, O_2^- and H_2O_2 in ORR process on the Pd sites, which is originally stronger than that on the Pt surface according to the volcano plot of ORR (Deming et al., 2015; Shao et al., 2006), facilitating the reaction kinetics and enhancing the intrinsic electrocatalysis for ORR. In principle, as the thickness of the shell continues to decrease, this electronic coupling should be more capable to weaken the adsorption energy of the oxygenated intermediates on Pd surfaces. However, the lattice expansion in the thin Pd shell induced by the Au core with relatively larger lattice parameters also becomes more prominent, leading to the upshift of the d-band position of Pd metal, which would harm its ORR activity by in turn enhancing

the adsorption of oxygenated intermediates on the same (Chen et al., 2016; Deming et al., 2015; Laskar and Skrabalak, 2016; Liu et al., 2021). Therefore, for completely making use of the advantages of thin Pd shell for ORR electrocatalysis, the disadvantaged lattice expansion should be averted for favorable adsorption of ORR intermediates. Nevertheless, both steadily obtaining core-shell structures with ultrathin shells and engineering them at the atomic level are hard and face great challenges (Chen et al., 2016; Xie et al., 2012, 2014).

We herein demonstrate a dual tailoring strategy to deliberately optimize the d-band position of Pd metal for boosting its performance in ORR electrocatalysis. In this strategy, we construct core-shell Au@NiPd nanoparticles with NiPd alloy shells of only three atomic layers by combining Au-catalyzed formation of core-shell Au@Ni nanoparticles with galvanic replacement reaction between Ni shells and Pd^{2+} precursors. In the final core-shell products, the Au core modifies the electronic configuration of Pd atoms through its bigger electronegativity, whereas the Ni atoms alloyed in the ultrathin shells neutralize the lattice stretching in Pd shells exerted by the Au cores, equipping the active Pd metal with an optimized d-band position favorable for the ORR electrocatalysis. In specific, the core-shell Au@NiPd nanoparticles at a Ni/Pd atomic ratio of 3/7 exhibit a half-wave potential of 0.92 V, specific activity of 3.7 mA cm^{-2}, and mass activity of 0.65 A mg^{-1} at 0.9 V versus reversible hydrogen electrode (RHE) for ORR in an alkaline medium, much better than those of their core-shell Au@Pd counterparts, commercial Pd/C and Pt/C catalysts, as well as the majority of the recent reported Pd-based electrocatalysts. Furthermore, as revealed by density functional theory (DFT) calculations, benefiting from the neutralization of Pd lattice expansion and the electronic coupling between Au and Pd, the adsorption energy of oxygenated intermediates on the sub-nano NiPd alloy shells weakens, promoting the hydrogenation of O* to *OH, which is the rate-determined step during ORR, and enhancing their ORR electrocatalytic behavior.

RESULTS AND DISCUSSION

Synthesis and characterizations of core-shell Au@NiPd nanoparticles with sub-nano NiPd alloy shells

As shown by the scheme in Figure 1A, a strategy that combines Au-catalyzed formation of core-shell Au@Ni nanoparticles with galvanic replacement reaction (GRR) between Ni shell and Pd^{2+} precursors was employed to gain sub-nano NiPd alloy shells on the Au cores. The Au seeds used in this strategy have an average size of 8.18 nm with a standard deviation of 1.75 nm, as evinced by the transmission electron microscopy (TEM) and high-resolution TEM images in Figure S1 as well as the histogram in Figure S2A of supplemental information. Then, with the assistance of Au catalysis we discovered before (Chen et al., 2016) that the Ni^{2+} ions are reduced and grow on the Au cores, forming core-shell Au@Ni nanoparticles with a Ni shell of up to three atomic layers. We initially used this Au catalysis strategy to prepare core-shell Au@Pd nanoparticles with Pd shells of up to three atomic layers in aqueous phase (Chen et al., 2016) and found that it is applicable for other core-shell systems in organic media. Analogous to the Au@Pd case in aqueous solution, for the Au@Ni system, after growing three Ni atomic layers in oleylamine on the Au cores, the surface property of the core-shell Au@Ni nanoparticles would resemble pure Ni particles, and lose its capability of catalytic reduction, ceasing the continuous reduction of Ni^{2+} precursors. The TEM image in Figure 1B and the corresponding histogram in Figure S2B demonstrate that these core-shell Au@Ni nanoparticles are quasi-spherical with an average size of 8.78 nm. As clearly observed in high-resolution aberration-corrected high-angle annular dark-field scanning TEM (HAADF-STEM) images in Figures 1C and S3A, the brightness contrast between the central and the extremely thin edge region of the particles indicates their typical core-shell feature with the ultrathin shell (Liu et al., 2021; Kim et al., 2017). The element mapping analyses of two arbitrarily selected particles shown in Figure $1D_1$ also indisputably confirms their core-shell construction (Figures $1D_2-D_4$). In addition, the lattice spacing of 0.195 nm at shell region and 0.233 nm at core region could be clearly identified from Figure 1C, corresponding to the (111) crystal facets of face-centered cubic (fcc) Ni and Au phases, respectively.

The ultrathin Ni shells of only three atomic layers would reduce the subsequently added Pd^{2+} ions under the reaction temperature depending on GRR between them (Figure 1A), which converts the thin Ni shells into sub-nano NiPd alloy shells and results in core-shell Au@NiPd nanoparticles with an alloy shell thickness of only three atomic layers. With different feeding amounts of Pd^{2+} ions, i.e., 0.00625, 0.0125 and 0.025 mmol, the actual Ni/Pd molar ratios in the alloy shells determined by inductively coupled plasma-atomic emission spectrometry (ICP-AES) are 9/1, 3/7, and 1/9 (as summarized in Table S1), corresponding to core-shell Au@Ni_xPd_y products labeled as Au@Ni_9Pd_1, Au@Ni_3Pd_7, and Au@Ni_1Pd_9, respectively. It is
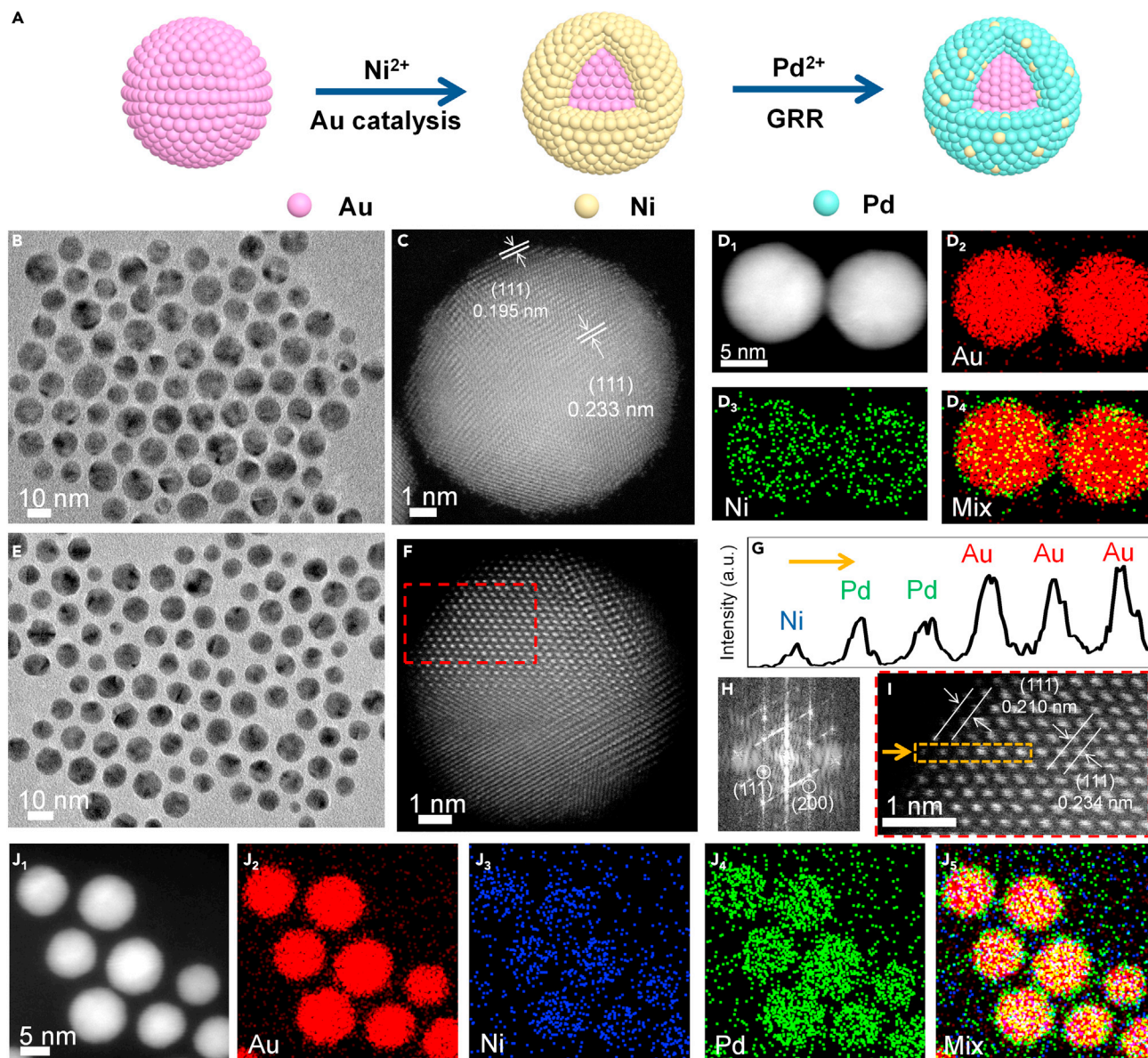
Figure 1. Synthetic Strategy and Characterizations of Core-shell Au@NiPd Nanoparticles

(A) Schematic illustration showing the combination of Au catalysis with galvanic replacement reaction for the formation of core-shell Au@NiPd nanoparticles with sub-nano NiPd alloy shells.

(B) TEM image of core-shell Au@Ni nanoparticles.

(C and D1) Aberration-corrected HAADF-STEM images of core-shell Au@Ni nanoparticles.

(D2–D4) Element mapping analyses of two arbitrarily selected core-shell Au@Ni nanoparticles shown in (D1).

(E) TEM image of core-shell Au@Ni$_3$Pd$_7$ nanoparticles.

(F and J1) Aberration-corrected HAADF-STEM images of core-shell Au@Ni$_3$Pd$_7$ nanoparticles.

(H) Fast Fourier transform image corresponding to the particle shown in (F).

(I) Magnified STEM image of the selective area of the particle shown in (F) encircled by red dotted line.

(G) Intensity profile along the yellow arrow direction from the selected area encircled by yellow dotted line shown in (I).

(J2–J5) Element mapping analyses of the arbitrarily selected core-shell Au@Ni$_3$Pd$_7$ nanoparticles shown in (J1).

noteworthy that, when Pd^{2+} and Ni^{2+} ions are simultaneously added into the reaction system with the existence of Au seeds, core-shell-shell Au@Pd@Ni nanoparticles would be formed as dominant products instead of core-shell Au@NiPd nanoparticles owing to the larger oxidation/reduction potential of Pd^{2+}/Pd than that of Ni^{2+}/Ni.

We take Au@Ni$_3$Pd$_7$ nanoparticles as typical examples to demonstrate the characterizations of their core-shell constructions and sub-nano features in their shell regions. As shown in Figures 1E and S2C, the conversion from Ni shells to NiPd alloy shells does not change the spherical morphologies of these core-shell nanoparticles and only leads to slight increase in average particle sizes (from 8.78 to 8.86 nm). The clear diffraction spots observed in fast Fourier transform image of the particle shown in Figure 1F verifies that the core-shell products generated from GRR between Ni shell and Pd^{2+} ions retain periodic structure and good crystallinity (Figure 1H). Analogously, the appeared brightness contrast from HAADF-STEM images of Figures 1F and S3B distinctly manifests that the shell thickness of the core-shell Au@NiPd nanoparticles is in the sub-nano scale. Their exact core-shell structure with an Au core and a NiPd alloy shell could be further uncovered by the element mapping analyses of the particles shown in Figure 1J$_1$, in which the signal of Au is concentrated on the central region of these particles (Figures 1J$_2$ and 1J$_5$), while the signals of both Pd and Ni are uniformly distributed on the particle margins (Figures 1J$_3$−1J$_5$). Furthermore, the alloy shell of only three atomic layers could be identified from the magnified HAADF-STEM image (Figure 1I) of the selected area encircled by the red dotted line shown in Figure 1F. Also, as clearly observed from the intensity profile of the yellow-dot-line encircled area (Figure 1G), along the direction indicated by the yellow arrow in Figure 1I, the NiPd alloy shell of only three atomic layers on Au core is determined. In addition, a (111) facet of NiPd alloy shells with lattice spacing of 0.210 nm and a (111) facet of Au cores with lattice spacing of 0.234 nm could also be discerned from Figure 1I. It should be noteworthy that the lattice spacing of alloy NiPd (111) crystal facet is smaller than that of pure Pd (111) crystal facet (0.225 nm) and that of Pd (111) crystal facet of core-shell Au@Pd nanoparticles (0.231 nm) synthesized by the Au-catalyzed strategy, as shown in Figure S4. Correspondingly, based on these lattice spacings, the lattice parameters of the sub-nano NiPd alloy shell and pure Pd shell on Au core were calculated to be 0.3637 nm and 0.4053 nm, respectively, which suggest that the contraction of Pd lattices is achieved in the sub-nano shells through alloying with Ni atoms.

The effect of Ni atoms in sub-nano shells on the contraction of Pd lattices could also be revealed by XRD patterns. As shown in Figure S5, the XRD patterns of both core-shell Au@Ni$_3$Pd$_7$ nanoparticles and core-shell Au@Pd nanoparticles show the typical diffraction peaks corresponding to face-centered cubic (fcc) phase. Owing to the ultrathin shell of only three atomic layers, the diffraction peaks of all core-shell samples are inevitably dominated by Au core. However, a discernible positive shift of the (111) diffraction peak for core-shell Au@Ni$_3$Pd$_7$ nanoparticles could be observed in comparison with that of core-shell Au@Pd nanoparticles, also illustrating that, to a certain extent, alloying with Ni atoms could neutralize the lattice tensile effect in Pd layer imposed by the Au cores.

The XPS spectra were employed to probe the surface composition of the as-synthesized core-shell samples and further explore the lattice tailoring in the sub-nano shells. As observed in Figure 2A, the 3d XPS spectra of Pd for all these samples could be deconvoluted into two pairs of doublets, corresponding to its metallic state at lower binding energy and oxidation state at higher binding energy, respectively (Chen et al., 2020; Huang et al., 2017; Wang et al., 2015). Of note, compared with those of commercial Pd/C catalyst, the Pd 3d peaks of core-shell Au@Pd have an apparent shift to lower values. In contrast, the Pd 3d peaks of core-shell Au@Ni$_3$Pd$_7$ nanoparticles exhibit a slight shift to higher values, which suggests that the lattice tensile effect in the sub-nano alloy shells induced by Au core with bigger lattice parameters has been neutralized (Chen et al., 2015, 2016; Deming et al., 2015; Laskar and Skrabalak, 2016). The reverse shift highlights the key role of Ni in regulating lattice strain effect in atomic level. Alloying with Ni atoms not only compensates the Pd lattice expansion induced by the Au core but also leads to slight shrinkage of its lattice spacing, which reversibly results in a mild increase of Au 4f binding energies for core-shell Au@Ni$_3$Pd$_7$ nanoparticles, as evinced by Figure 2B. The variation of the lattice characteristics inevitably changes the d-band position of Pd in these samples. As shown in the surface valence spectra of Figure 2C, compared with that of commercial Pd/C catalyst, the lattice expansion upshifts the d-band position of Pd of core-shell Au@Pd nanoparticles (Chen et al., 2015, 2016), while the lattice contraction in the sub-nano NiPd alloy shells lowers the d-band position of Pd of core-shell Au@Ni$_3$Pd$_7$ nanoparticles. Furthermore, Ni atoms in sub-nano alloy shell also would cause the electron effect, leading to the electron to flow from Pd atoms to Ni atoms due to more d-band vacancies of Ni than that of Pd (Xu et al., 2013), which also would lower the d-band position of Pd. The change of d-band center of Pd could be demonstrated by the electrochemical reduction of PdO shown in Figure 2D (Liu et al., 2014). The most positive reduction peak potential (ca. 804 mV) in cyclic voltammogram (CV) curves of core-shell Au@Ni$_3$Pd$_7$ relative to that in CVs of core-shell Au@Pd (ca. 795 mV) and commercial Pd/C catalyst (ca. 650 mV) illustrates the weakest adsorption energy of hydroxyl on
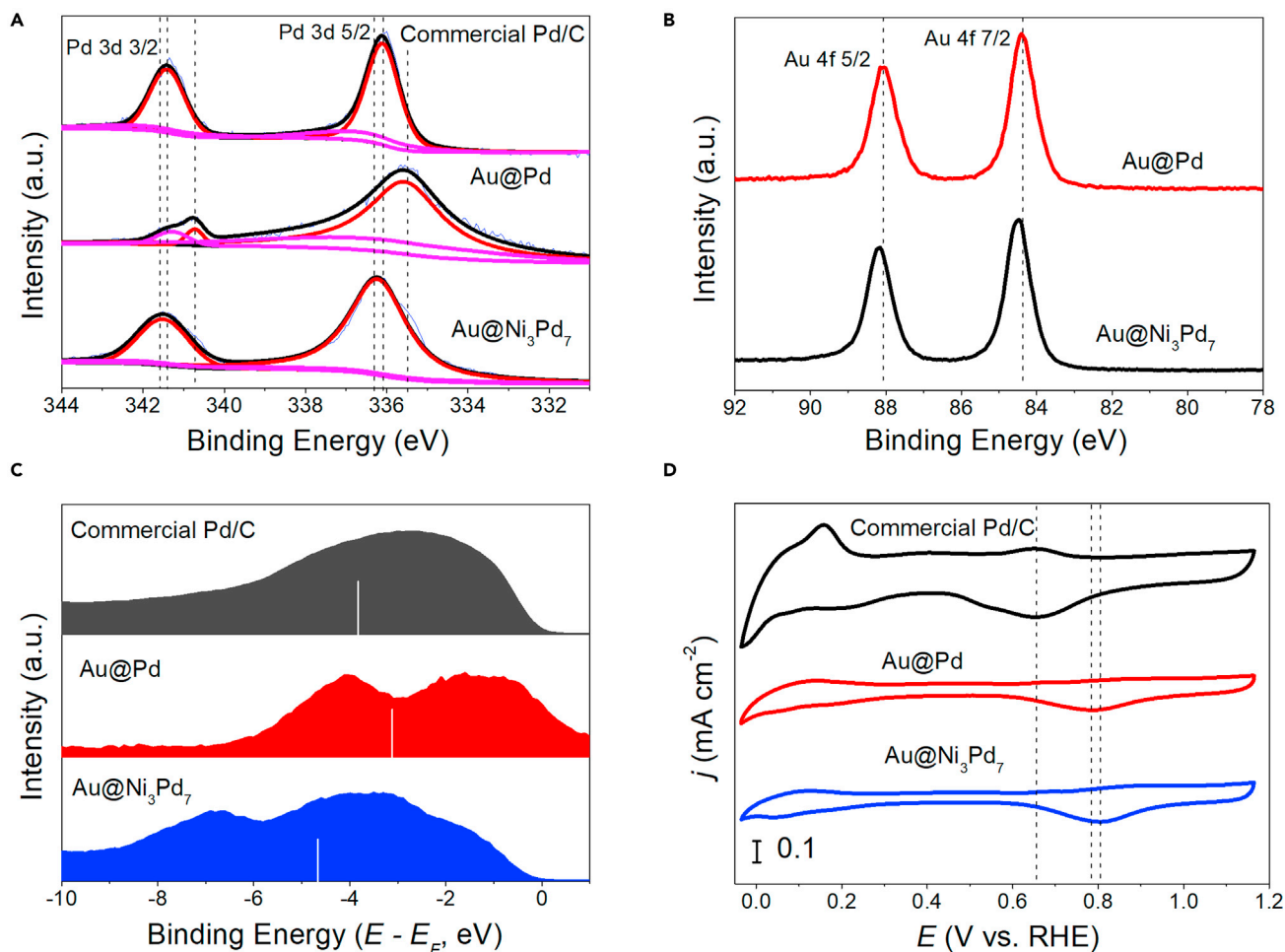
Figure 2. XPS and Electrochemical Characterizations of Core-shell Nanoparticles

(A) Pd 3d XPS spectra of core-shell $Au@Ni_3Pd_7$ nanoparticles, core-shell Au@Pd nanoparticles, and commercial Pd/C catalyst.

(B) Au 4f XPS spectra of core-shell $Au@Ni_3Pd_7$ nanoparticles and core-shell Au@Pd nanoparticles.

(C) Surface valence spectra of core-shell $Au@Ni_3Pd_7$ nanoparticles, core-shell Au@Pd nanoparticles, and commercial Pd/C catalyst.

(D) Cyclic voltammogram (CV) curves in 0.1 M KOH at a scan rate of 50 mV s^{-1} for core-shell $Au@Ni_3Pd_7$ nanoparticles, core-shell Au@Pd nanoparticles, and commercial Pd/C catalyst.

the NiPd alloy surface. Interesting, core-shell Au@Pd nanoparticles also possess a more positive potential than that of commercial Pd/C catalyst for the reduction of PdO species, and this could be attributed to the strong electronic coupling between their Au core and ultrathin Pd shell regions (Fu et al., 2014). Similarly, the CO stripping curve of core-shell $Au@Ni_3Pd_7$ nanoparticles appears an obvious negative shift (Figure S6), also supporting the weak adsorption energy of oxygenated species on their Pd sites. In addition, the ECSAs based on the integral areas of corresponding CO stripping peaks shown in Figure S6 are calculated to be 118.1 m^2 g^{-1} for core-shell $Au@Ni_3Pd_7$ nanoparticles, 60.1 m^2 g^{-1} for core-shell Au@Pd nanoparticles, and 80.0 m^2 g^{-1} for commercial Pd/C catalyst, respectively. Because of almost exactly the same size for core-shell $Au@Ni_3Pd_7$ nanoparticles and core-shell Au@Pd nanoparticles, as well as the dilution effect of Ni atoms on the Pd site in alloy shells, the larger ESCA of core-shell $Au@Ni_3Pd_7$ nanoparticles just manifests the presence of higher ratio of the electrochemically active sites on the sub-nano NiPd alloy shells relative to that on the pure Pd shells.

Electrochemical measurements for ORR on core-shell Au@NiPd nanoparticles

The electrocatalytic properties of core-shell $Au@Ni_3Pd_7$ nanoparticles for ORR in alkaline media were evaluated and benchmarked against core-shell Au@Pd nanoparticles, commercial Pd/C, and commercial Pt/C catalysts. The ORR polarization curves of these catalysts were obtained by performing the LSV in O$_2$-

saturated 0.1 M KOH. As clearly shown in Figure 3A, both of the core-shell Au@Pd nanoparticles with or without the Ni atoms in the sub-nano shells exhibit higher half-wave potentials (0.92 and 0.88 V for core-shell Au@Ni$_3$Pd$_7$ nanoparticles and core-shell Au@Pd nanoparticles, respectively) not only relative to commercial Pd/C catalyst (0.81 V), even relative to commercial Pt/C catalysts (0.86 V), demonstrating the superiority of core-shell nanostructures for electrochemically catalyzing O$_2$ reduction. Furthermore, the larger half-wave potential of core-shell Au@Ni$_3$Pd$_7$ nanoparticles than that of core-shell Au@Pd nanoparticles indicates the positive effect of Ni atoms in the alloy shells on boosting the ORR performance of Pd sites. Figure 3B compares the current densities of these four catalysts normalized by the geometric area of electrode (specific activity) and by the mass of Pd loaded on the electrode (mass activity) at 0.9 V for ORR. As expected, core-shell Au@Ni$_3$Pd$_7$ nanoparticles show the mass activity of 0.63 A mg^{-1} at 0.9 V and is 3.3, 5.9, and 13.0 times higher than that of core-shell Au@Pd nanoparticles (0.2 A mg^{-1}), commercial Pt/C catalyst (0.11 A mg^{-1}), and commercial Pd/C catalyst (0.05 A mg^{-1}), respectively. Also, the specific activity of core-shell Au@Ni$_3$Pd$_7$ nanoparticles for ORR reaches to 3.7 mA cm^{-2} at 0.9 V, which is much higher than 2.5 mA cm^{-2} of core-shell Au@Pd nanoparticles, 2.1 mA cm^{-2} of commercial Pt/C catalyst, and 0.9 mA cm^{-2} of commercial Pd/C catalyst. In addition, the enhanced mass activity and specific activity of Au@Ni$_3$Pd$_7$ nanoparticles also surpass the majority of the recently reported Pd-even Pt-based ORR electrocatalysts, as summarized in Table S2. The smallest Tafel slope of core-shell Au@Ni$_3$Pd$_7$ nanoparticles (73 mV dec^{-1}) among these four catalysts suggests the fastest ORR kinetics on their sub-nano NiPd alloy shells, as displayed in Figure 3C. The Nyquist plots of EIS disclose that the core-shell Au@Ni$_3$Pd$_7$ nanoparticles possess a much smaller semicircle diameter than other reference catalysts (Figure 3D), which represents a lower electron transfer resistance during ORR. Moreover, the equivalent circuit of the electrochemical interface has been depicted as shown in the inset of Figure 3D. The circuit includes an electrolyte resistance (Rs), charge transfer resistance (Rct), and Q associated with a constant phase element corresponding to the double layer capacitance. The values of Rct for core-shell Au@Ni$_3$Pd$_7$ nanoparticles, core-shell Au@Pd nanoparticles, commercial Pt/C catalyst, and commercial Pd/C catalyst were determined to be 131, 320, 750, and 2,419 Ω cm^{-2}, respectively. The lowest Rct value of core-shell Au@Ni$_3$Pd$_7$ nanoparticles again demonstrates their fastest electron transfer during ORR. The favorable reaction kinetics and fast electron transfer equip the core-shell Au@Ni$_3$Pd$_7$ nanoparticles with excellent electrocatalytic behavior toward ORR, vividly demonstrating that the dual tailoring on electronic coupling and lattice strain effect could effectively boost the electrocatalysis of Pd sites for ORR.

For assessing the ORR pathway on the sub-nano NiPd alloy shells, polarization curves were recorded at different rotating speeds (Figure 3E). The nearly parallel Koutecky-Levich (K-L) plots inserted in Figure 3E suggest the first-order reaction kinetics toward the oxygen dissolved in the electrolyte. According to the K-L equation, the electron-transfer number (n) is determined to be 3.9 to 4.1 over the whole potential range, indicating that the four-electron pathway is dominant for ORR on the sub-nano NiPd alloy shells of core-shell Au@Ni$_3$Pd$_7$ nanoparticles. Moreover, as shown in Figure S7, in the selected potential range, the calculated peroxide yield of core-shell Au@Ni$_3$Pd$_7$ nanoparticles during ORR remains below 1.5%, corresponding to their high electron-transfer number for ORR. In addition to their remarkable activity, the core-shell Au@Ni$_3$Pd$_7$ nanoparticles also have exceptional electrocatalytic durability for ORR. As shown in Figure 3F, after undergoing an accelerated durability test for 10,000 cycles, the core-shell Au@Ni$_3$Pd$_7$ nanoparticles have little changes in half-wave potential and specific activity at 0.9 V for ORR, which are much better than those of commercial Pt/C catalyst (Figure S8A). Based on their CO stripping peak (Figures S8B and S8C), the ECSA of core-shell Au@Ni$_3$Pd$_7$ nanoparticles after the accelerated durability test only decreases by 6.9% (Figure S8D) and is much lower than that of commercial Pt/C catalyst after the accelerated durability test (34.8%). Moreover, the core-shell construction and surface composition are also maintained for core-shell Au@Ni$_3$Pd$_7$ nanoparticles after the accelerated durability test, as proved by the microscopic images in Figure S9 and the ICP-AES data in Table S1, which guarantee them to continuously and stably catalyze the reduction of oxygen molecules.

For full transparency of this study, we also evaluated the electrocatalytic performance of core-shell Au@Ni$_3$Pd$_7$ nanoparticles for ORR in an acidic medium (0.1 M HClO$_4$). Unfortunately, as shown in Figure S10, different from the highly efficient electrocatalysis for ORR in the alkaline electrolyte, the current density of core-shell Au@Ni$_3$Pd$_7$ nanoparticles for ORR in the acidic medium is lower than that of commercial Pt/C catalyst, illustrating that the electron effect and lattice strain in the sub-nano NiPd alloy shells cannot significantly promote the originally sluggish reaction kinetics of ORR on Pd sites in the acidic conditions. Therefore, the core-shell Au@Ni$_3$Pd$_7$ nanoparticles currently developed in this work are only suitable for the ORR in alkaline media.
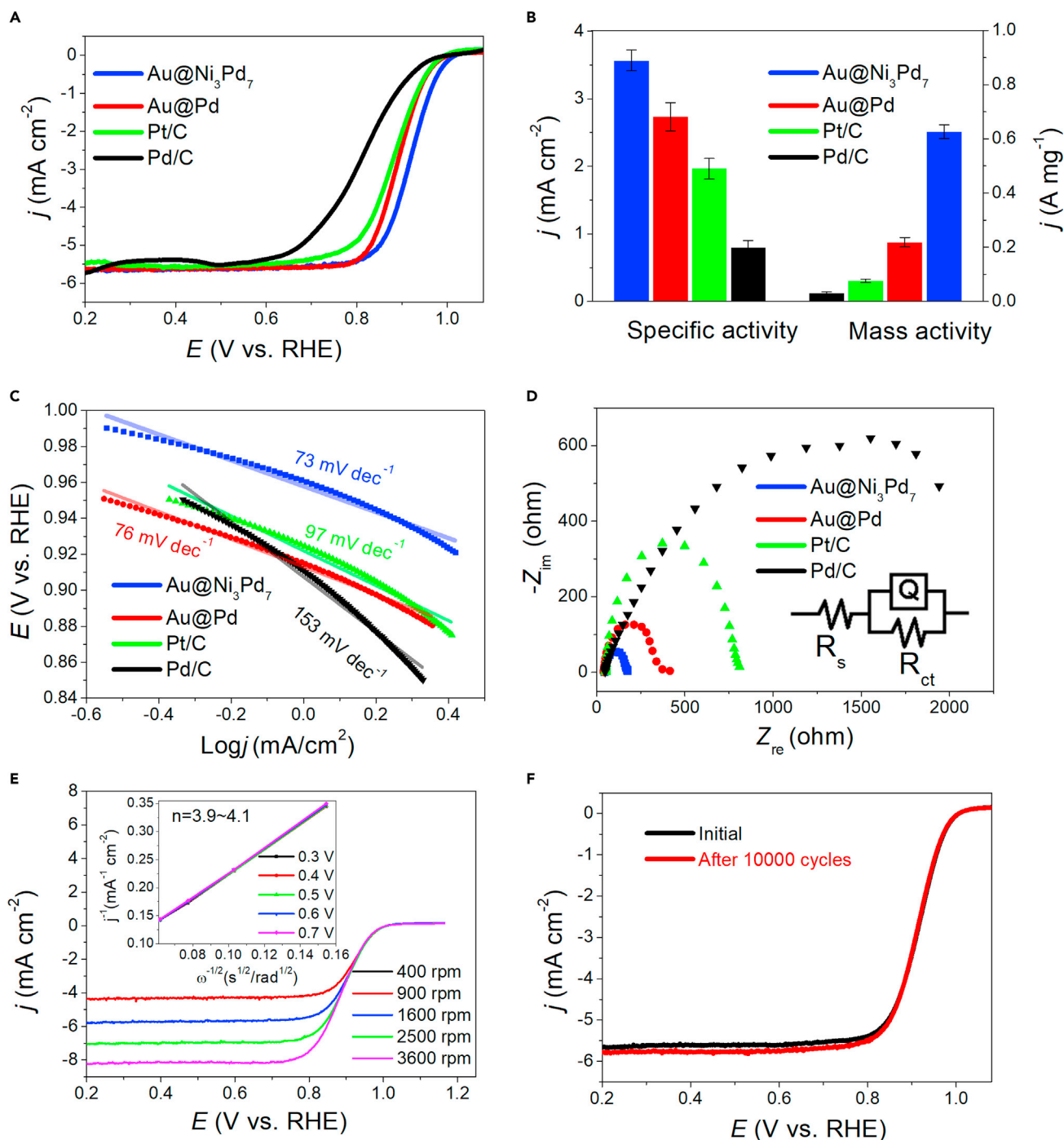
Figure 3. Electrochemical Measurements for Oxygen Reduction Reaction (ORR)

(A) ORR polarization curves of core-shell Au@Ni$_3$Pd$_7$ nanoparticles, core-shell Au@Pd nanoparticles, commercial Pd/C catalyst, and commercial Pt/C catalyst at room temperature in O2-saturated 0.1 M KOH at a scan rate of 10 mV s^{-1} and a rotating speed of 1,600 rpm.

(B) Column diagrams of mass activity and specific activity of different catalysts at 0.9 V.

(C) Tafel plots over core-shell Au@Ni$_3$Pd$_7$ nanoparticles, core-shell Au@Pd nanoparticles, commercial Pd/C catalyst, and commercial Pt/C catalyst in 0.1 M KOH.

(D) Nyquist plots of EIS over core-shell Au@Ni$_3$Pd$_7$ nanoparticles, core-shell Au@Pd nanoparticles, commercial Pd/C catalyst, and commercial Pt/C catalyst in 0.1 M KOH.

(E) ORR polarization curves of core-shell Au@Ni$_3$Pd$_7$ nanoparticles at different rotating speeds.

(F) ORR polarization curves of core-shell Au@Ni$_3$Pd$_7$ nanoparticles before and after 10,000 cycles.
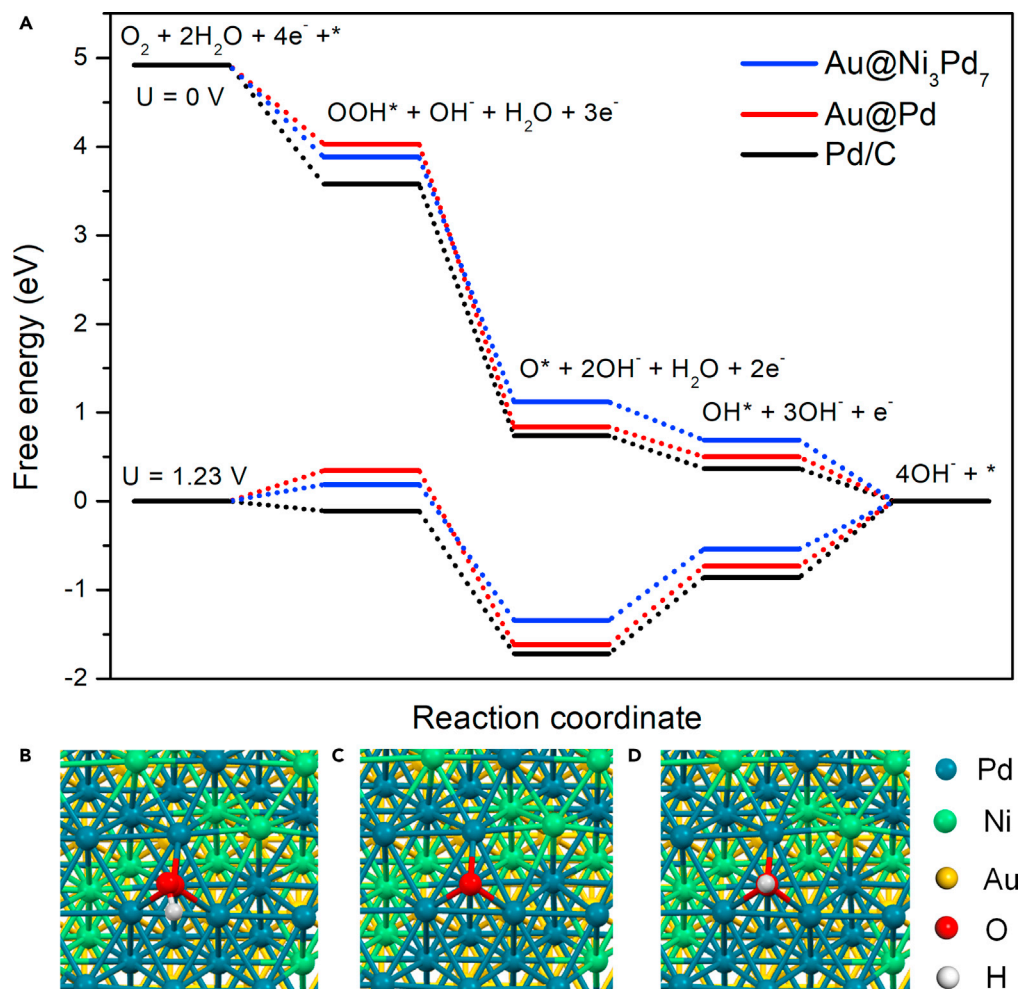
Figure 4. DFT Computational Investigations

(A) Free energy diagram of ORR over core-shell $Au@Ni_3Pd_7$ nanoparticles, core-shell Au@Pd nanoparticles, and commercial Pd/C catalyst at 0 and 1.23 V.

(B−D) The adsorbed model of intermediates OOH*, O*, and OH* on the surface of core-shell $Au@Ni_3Pd_7$ nanoparticles.

Theoretical investigations into the ORR on core-shell Au@NiPd nanoparticles with sub-nano NiPd alloy shells

DFT calculations were carried out to gain insights into the mechanism of ORR on core-shell $Au@Ni_3Pd_7$ nanoparticles. As clearly shown in the free energy diagram for ORR over core-shell $Au@Ni_3Pd_7$ nanoparticles, core-shell Au@Pd nanoparticles, and commercial Pd/C catalyst (Figure 4A), when no extra potential is applied, the free energy of every elementary reaction for ORR on these three catalysts gradually decreases at 0 V (Figures 4 and S11). While at the equilibrium potential of 1.23 V, the hydrogenation of O* to form OH* on the surface of these three catalysts must overcome the highest energy barrier originating from too strong adsorption of oxygenated intermediates generated during ORR process, which is the most seriously endothermic process as the rate-determined step for ORR on these catalysts. The lowest increase of free energy for the step on the sub-nano alloy shell surfaces of core-shell $Au@Ni_3Pd_7$ nanoparticles illustrates their best electrocatalytic performance toward ORR compared with their core-shell Au@Pd counterparts and commercial Pd catalyst. Besides the electronic coupling between Au and Pd, the Ni atoms alloyed in the sub-nano alloy shell that leads to shrinkage of the Pd lattices further lower the adsorption energy of oxygenated intermediates in ORR on Pd sites (Figures 4B−4D), which facilitates the hydrogenation of O* to OH* and enhances the ORR activity of core-shell $Au@Ni_3Pd_7$ nanoparticles. An appropriate molar ratio of Ni/Pd is necessary for the sub-nano NiPd alloy shells to have the optimal ORR performance. As shown in Figure S12 and Table S3, the above-mentioned core-shell $Au@Ni_3Pd_7$ nanoparticles show the

maximum activity and half-wave potential for ORR, compared with the core-shell Au@NiPd nanoparticles with other Ni/Pd molar ratios in their sub-nano alloy shells. It is easy to understand that smaller amount of Ni atoms in the NiPd alloy shells cannot sufficiently neutralize the tensile effect in Pd lattices imposed by Au core, leading to limited decrease of the adsorption energy of oxygenated species on the Pd sites, while the excess amount of Ni atoms would not only dilute the Pd sites but also unduly weaken the adsorption energy of the oxygenated intermediates on the same, which may deteriorate the ORR by impeding the activation of initial oxygen molecules.

DISCUSSION

In this work, core-shell Au@NiPd nanoparticles with sub-nano NiPd alloy shells of only three atomic layers were successfully constructed by combining the Au-catalyzed formation of core-shell Au@Ni nanoparticles with galvanic replacement reaction between pre-formed Ni shells and Pd^{2+} precursors. The as-prepared core-shell Au@NiPd nanoparticles at a Ni/Pd molar ratio of 3/7 ($Au@Ni_3Pd_7$) show much higher mass activity and specific activity for ORR compared with core-shell Au@Pd nanoparticles, commercial Pd/C catalyst, and commercial Pt catalyst. In addition, the nearly unchanged half-wave potential and specific activity at 0.9 V before and after the accelerated durability test for 10,000 cycles also verify their superior electrocatalytic durability. DFT calculations reveal that, benefiting from the weakened adsorption energy of oxygenated species on the Pd sites due to electronic coupling and lattice strain regulation, the hydrogenation of O* to form OH* for ORR on the core-shell $Au@Ni_3Pd_7$ nanoparticles is prompted, significantly boosting their electrocatalysis for oxygen reduction reaction.

Limitations of the study

For this study, it is difficult to accurately quantify the electron effect between the Au core and Pd shell, and lattice strain of Pd shell imposed by the Au core and the doped Ni atoms in alloy shell, owing to the mutual influence among them. In addition, the poor electrocatalytic activity of core-shell Au@NiPd nanoparticles for ORR in acidic media is also a nonnegligible limitation for this study.

STAR★METHODS

Detailed methods are provided in the online version of this paper and include the following:

- KEY RESOURCES TABLE
- RESOURCE AVAILABILITY
  - Lead contact
  - Materials availability
  - Data and code availability
- METHODS DETAILS
  - Synthesis of core-shell Au@NiPd nanoparticles
  - Synthesis of core-shell Au@Pd nanoparticles
  - Particle characterizations
  - Electrochemical measurements
  - Calculation details

SUPPLEMENTAL INFORMATION

Supplemental information can be found online at https://doi.org/10.1016/j.isci.2021.103332.

AUTHOR CONTRIBUTIONS

J.Y. and D.C. conceived the idea and, with L.X., designed the experiments. Q.Z. and D.L. performed the main materials synthesis measurements. H.L. and D.C. performed the TEM test and analysis. D.C. was responsible for the DFT calculation and analysis. C.H., P.C., and X.W. assisted in the materials synthesis. D.C., Q.Z., and J.Y. analyzed the data and wrote the manuscript. All the authors discussed the manuscript.

SUPPORTING CITATIONS

The following references appear in the supplemental information: Bampos et al. (2020); Bhalothia et al. (2020a); Bhalothia et al. (2020b); Chen et al. (2019); Gong et al. (2019); Guo et al. (2018); He et al. (2019); Huang et al. (2020); Hussain et al. (2019); Jo et al. (2021); Li et al. (2021); Lüsi et al. (2020); Meléndez-González et al. (2020); Pang et al. (2021); Roy et al. (2020); Shen et al. (2019); Vega-Cartagena et al. (2019); Wang et al. (2018a, 2018b); Wang et al. (2021); Xie et al. (2021).

REFERENCES

Antolini, E. (2009). Palladium in fuel cell catalysis. Energy Environ. Sci. 2, 915–931.

Bampos, G., Sygellou, L., and Bebelis, S. (2020). Oxygen reduction reaction activity of Pd-based bimetallic electrocatalysts in alkaline medium. Catal. Today 355, 685–697.

Bhalothia, D., Chen, P.-C., Yan, C., Yeh, W., Tsai, D.-L., Chan, T.-S., Wang, K.-W., and Chen, T.-Y. (2020a). Heterogeneous assembly of Pt-clusters on hierarchically structured CoO$_x$@SnPd$_2$@SnO$_2$ quaternary nanocatalysts manifesting oxygen reduction reaction performance. New J. Chem. 44, 9712–9724.

Bhalothia, D., Tsai, D.-L., Wang, S.-P., Yan, C., Chan, T.-S., Wang, K.-W., Chen, T.-Y., and Chen, P.-C. (2020b). Ir-oxide mediated surface restructure and corresponding impacts on durability of bimetallic NiOx@Pd nanocatalysts in oxygen reduction reaction. J. Alloys Compd. 844, 156160.

Bu, L., Guo, S., Zhang, X., Shen, X., Su, D., Lu, G., Zhu, X., Yao, J., Guo, J., and Huang, X. (2016). Surface engineering of hierarchical platinum cobalt nanowires for efficient electrocatalysis. Nat. Commun. 7, 11850.

Bu, L., Shao, Q., Pi, Y., Yao, J., Luo, M., Lang, J., Hwang, S., Xin, H., Huang, B., Guo, J., et al. (2018). Coupled s-p-d exchange in facet-controlled Pd$_3$Pb tripods enhances oxygen reduction catalysis. Chem 4, 359–371.

Chen, H.Y., Jin, M.X., Zhang, L., Wang, A.J., Yuan, J., Zhang, Q.L., and Feng, J.J. (2019). One-pot aqueous synthesis of two-dimensional porous bimetallic PtPd alloyed nanosheets as highly active and durable electrocatalyst for boosting oxygen reduction and hydrogen evolution. J. Colloid Interface Sci. 543, 1–8.

Chen, D., Li, J., Cui, P., Liu, H., and Yang, J. (2016). Gold-catalyzed formation of core-shell gold-palladium nanoparticles with palladium shells up to three atomic layers. J. Mater. Chem. A 4, 3813–3821.

Chen, D., Li, C., Liu, H., Ye, F., and Yang, J. (2015). Core-shell Au@Pd nanoparticles with enhanced catalytic activity for oxygen reduction reaction via core-shell Au@Ag/Pd constructions. Sci. Rep. 5, 11949.

Chen, Y., Li, Z., Zhu, Y., Sun, D., Liu, X., Xu, L., and Tang, Y. (2019b). Atomic Fe dispersed on N-doped carbon hollow nanospheres for high-efficiency electrocatalytic oxygen reduction. Adv. Mater. 31, 1806312.

Chen, D., Sun, P., Liu, H., and Yang, J. (2017). Bimetallic Cu-Pd alloy multipods and their highly electrocatalytic performance for formic acid oxidation and oxygen reduction. J. Mater. Chem. A 5, 4421–4429.

Chen, D., Wang, Y., Liu, D., Liu, H., Qian, C., He, H., and Yang, J. (2020). Surface composition dominates the electrocatalytic reduction of CO$_2$ on ultrafine CuPd nanoalloys. Carbon Energy 2, 443–451.

Chen, D., Xu, L., Liu, H., and Yang, J. (2019a). Rough-surfaced bimetallic copper-palladium alloy multicubes as highly bifunctional electrocatalysts for formic acid oxidation and oxygen reduction. Green. Energy Environ. 4, 254–263.

Deming, C.P., Zhao, A., Song, Y., Liu, K., Khan, M.M., Yates, V.M., and Chen, S. (2015). Alkyne-protected AuPd alloy nanoparticles for electrocatalytic reduction of oxygen. ChemElectroChem 2, 1719.

Fu, G., Liu, Z., Chen, Y., Lin, J., Tang, Y., and Lu, T. (2014). Synthesis and electrocatalytic activity of Au@Pd core-shell nanothorns for the oxygen reduction reaction. Nano Res. 7, 1205–1214.

Gong, Q., Gong, S., Zhang, T., Cheng, X., and Li, H. (2019). Achieving high activity and stability of carbon supported Pd-Cu alloyed catalysts for fuel cell applications. J. Electrochem. Soc. 166, F906–F913.

Guo, H., Wen, D., Wang, T., Fan, X., Song, L., Gong, H., Xia, W., Gao, B., Li, L., and He, J. (2018). In situ palladium/nitrogen-doped ordered mesoporous carbon hybrids as highly active and durable electrocatalysts for oxygen reduction reaction. J. Porous Mater. 26, 371–379.

Guo, S., Zhang, X., Zhu, W., He, K., Su, D., Mendoza-Garcia, A., Ho, S.F., Lu, G., and Sun, S. (2014). Nanocatalyst superior to Pt for oxygen reduction reactions: the case of core/shell Ag(Au)/CuPd nanoparticles. J. Am. Chem. Soc. 136, 15026–15033.

He, X., Li, D., Bai, Z., Chang, F., Qiao, J., and Yang, L. (2019). Multi-wall carbon nanotube-supported palladium-cobalt oxide nanoparticle as efficient catalyst for oxygen reduction reaction. Ionics 25, 5929–5937.

Huang, S., Lu, S., Hu, H., Cao, B., Li, H., Duan, F., Zhu, H., Gu, H., and Du, M. (2020). A stable PdCu@Pd core-shell nanobranches with enhanced activity and methanol-tolerant for oxygen reduction reaction. Electrochim. Acta 354, 136680.

Huang, W., Ma, X.-Y., Wang, H., Feng, R., Zhou, J., Duchesne, P.N., Zhang, P., Zhou, J., Cai, W.-B., and Li, Y. (2017). Promoting effect of Ni(OH)$_2$ on palladium nanocrystals leads to greatly improved operation durability for electrocatalytic ethanol oxidation in alkaline solution. Adv. Mater. 29, 1703057.

Hussain, S., Erikson, H., Kongi, N., Tarre, A., Ritslaid, P., Kook, M., Rähn, M., Merisalu, M., Sammelselg, V., and Tammeveski, K. (2019). Improved ORR activity and long-term durability of Pt nanoparticles deposited on TiO2-decorated multiwall carbon nanotubes. J. Electrochem. Soc. 166, F1284–F1291.

Jiang, G., Zhu, H., Zhang, X., Shen, B., Wu, L., Zhang, S., Lu, G., Wu, Z., and Sun, S. (2015). Core/shell face-centered tetragonal FePd/Pd nanoparticles as an efficient non-Pt catalyst for the oxygen reduction reaction. ACS Nano 9, 11014–11022.

Jiang, J., Ding, W., Li, W., and Wei, Z. (2020). Freestanding single-atom-layer Pd-basedcatalysts: oriented splitting of energy bands for unique stability and activity. Chem 6, 431–447.

Jo, H.-G., Kim, K.-H., and Ahn, H.-J. (2021). Nitrogen-doped carbon quantum dots decorated on platinum catalysts for improved oxygen reduction reaction. Appl. Surf. Sci. 554, 149594.

Kakati, N., Maiti, J., Lee, S.H., Jee, S.H., Viswanathan, B., and Yoon, Y.S. (2014). Anode catalysts for direct methanol fuel cells in acidic media: do we have any alternative for Pt or Pt—Ru? Chem. Rev. *114*, 12397–12429.

Kim, D., Xie, C., Beckne, N., Yu, Y., Karamad, M., Chan, K., Crumlin, E.J., Nørskov, J.K., and Yang, P. (2017). Electrochemical activation of CO₂ through atomic ordering transformations of AuCu nanoparticles. J. Am. Chem. Soc. *139*, 8329–8336.

Koenigsmann, C., Scofield, M.E., Liu, H., and Wong, S.S. (2012). Designing enhanced one-dimensional electrocatalysts for the oxygen reduction reaction: probing size- and composition-dependent electrocatalytic behavior in noble metal nanowires. J. Phys. Chem. Lett. *3*, 3385–3398.

Koenigsmann, C., and Wong, S.S. (2011). One-dimensional noble metal electrocatalysts: a promising structural paradigm for direct methanol fuel cells. Energy Environ. Sci. *4*, 1161–1176.

Kresse, G., and Furthmüller, J. (1996a). Efficiency of Ab-Initio total energy calculations for metals and semiconductors using a plane-wave basis set. Comput. Mater. Sci. *6*, 15–50.

Kresse, G., and Furthmüller, J. (1996b). Efficient iterative schemes for Ab Initio total-energy calculations using a plane-wave basis set. Phys Rev B Condens. Matter *54*, 11169–11186.

Kresse, G., and Joubert, D. (1999). From ultrasoft pseudopotentials to the projector augmented-wave method. Phys. Rev. B *59*, 1758–1775.

Laskar, M., and Skrabalak, S.M. (2016). A balancing act: manipulating reactivity of shape-controlled metal nanocatalysts through bimetallic architecture. J. Mater. Chem. A *4*, 6911–6918.

Li, B., and Prakash, J. (2009). Oxygen reduction reaction on carbon supported Palladium-Nickel alloys in alkaline media. Electrochem. Commun. *11*, 1162–1165.

Li, J., Sun, X., Duan, Y., Jia, D., Li, Y., and Wang, J. (2021). Enhanced oxygen reduction reaction performance over Pd catalysts by oxygen-surface-modified SiC. Chin. J. Catal. *42*, 963–970.

Lüsi, M., Erikson, H., Sarapuu, A., Merisalu, M., Rähn, M., Treshchalov, A., Paiste, P., Käärik, M., Leis, J., Sammelselg, V., et al. (2020). Electroreduction of oxygen on carbide-derived carbon supported Pd catalysts. ChemElectroChem *7*, 546–554.

Li, M., Zhao, Z., Cheng, T., Fortunelli, A., Chen, C.-Y., Yu, R., Zhang, Q., Gu, L., Merinov, B.V., and Lin, Z. (2016). Ultrafine jagged platinum nanowires enable ultrahigh mass activity for the oxygen reduction reaction. Science *354*, 1414–1419.

Liu, H.-M., Han, S.-H., Zhu, Y.-Y., Chen, P., and Chen, Y. (2018). Reduced graphene oxide supported PdNi alloy nanocrystals for the oxygen reduction and methanol oxidation reactions. Green. Energy Environ. *3*, 375–383.

Liu, H., Koenigsmann, C., Adzic, R.R., and Wong, C. (2014). Probing ultrathin one-dimensional Pd-

Ni nanostructures as oxygen reduction reaction catalysts. ACS Catal. *4*, 2544–2555.

Liu, D., Zeng, Q., Liu, H., Hu, C., Chen, D., Xu, L., and Yang, J. (2021). Combining the core-shell construction with an alloying effect for high efficiency ethanol electrooxidation. Cell Rep. Phys. Sci. *2*, 100357.

Lu, X., Ahmadi, M., DiSalvo, F.J., and Abruña, H. (2020). Enhancing the electrocatalytic activity of Pd/M (M = Ni, Mn) nanoparticles for the oxygen reduction reaction in alkaline media through electrochemical dealloying. ACS Catal. *10*, 5891–5898.

Lu, F., Zhang, Y., Liu, S., Lu, D., Su, D., Liu, M., Zhang, Y., Liu, P., Wang, J., Adzic, R.R., and Gang, O. (2017). Surface proton transfer promotes four-electron oxygen reduction on gold nanocrystal surfaces in alkaline solution. J. Am. Chem. Soc. *139*, 7310–7317.

Meléndez-González, P.C., Garza-Duran, E., Martínez-Loyola, J.C., Quintana-Owen, P., Alonso-Lemus, I.L., and Rodríguez-Varela, F.J. (2020). Enhanced catalytic activity of low-Pt content nanocatalysts supported on hollow carbon spheres for the ORR in alkaline media. MRS Adv. *5*, 2961–2972.

Monkhorst, H.J., and Pack, J.D. (1976). Special points for brillouin-zone integrations. Phys. Rev. B *13*, 5188–5192.

Neergat, M., Gunasekar, V., and Rahul, R. (2011). Carbon-supported Pd-Fe electrocatalysts for oxygen reduction reaction (ORR) and their methanol tolerance. J. Electroanal. Chem. *658*, 25–32.

Noha, S., and Shim, J.H. (2016). Asymmetric Au-core Pd-shell nanoparticles supported on reduced graphene oxide for enhanced electrocatalytic activity. RSC Adv. *6*, 84334–84341.

Pang, L., Miao, Y., Bhange, S.N., Barras, A., Addad, A., Roussel, P., Amin, M.A., Kurungot, S., Szunerits, S., and Boukherroub, R. (2021). Enhanced electrocatalytic activity of PtRu/nitrogen and sulphur Co doped crumbled graphene in acid and alkaline media. J. Colloid Interface Sci. *590*, 154–163.

Perdew, J.P., Burke, K., and Ernzerhof, M. (1996). Generalized gradient approximation made simple. Phys. Rev. Lett. *77*, 3865–3868.

Roy, N., Yasmin, S., Ejaz, A., Han, H.S., and Jeon, S. (2020). Influence of pyrrolic and pyridinic-N in the size and distribution behaviour of Pd nanoparticles and ORR mechanism. Appl. Surf. Sci. *533*, 147500.

Shao, M.-H., Sasaki, K., and Adzic, R.R. (2006). Pd-Fe nanoparticles as electrocatalysts for oxygen reduction. J. Am. Chem. Soc. *128*, 3526–3527.

Shao, Q., Wang, P., Zhu, T., and Huang, X. (2019). Low dimensional platinum-based bimetallic nanostructures for advanced catalysis. Acc. Chem. Res. *52*, 3384–3396.

Shen, Y., Shi, D., Liu, L., Liao, F., Zhu, W., and Shao, M. (2019). Pd nanoparticles/F, N Co doping graphene composites for oxygen reduction and zinc-air batteries. ACS Sustain. Chem. Eng. *7*, 12281–12287.

Shim, J.H., Kim, J., Lee, C., and Lee, Y. (2011). Porous Pd layer-coated Au nanoparticles supported on carbon: synthesis and electrocatalytic activity for oxygen reduction in acid media. Chem. Mater. *23*, 4694–4700.

Sonika, P.S., Gangadharan, P.K., Khan, Z., Kurungot, S., and Jaiswal, A. (2019). Cubic palladium nanorattles with solid octahedron gold core for catalysis and alkaline membrane fuel cell applications. ChemCatChem *11*, 4383–4392.

Tao, L., Huang, B., Jin, F., Yang, Y., Luo, M., Sun, M., Liu, Q., Gao, F., and Guo, S. (2020). Atomic PdAu interlayer sandwiched into Pd/Pt core/shell nanowires achieves superstable oxygen reduction catalysis. ACS Nano *14*, 11570–11578.

Vega-Cartagena, M., Flores-Vélez, E.M., Colón-Quintana, G.S., Blasini Pérez, D.A., De Jesús, M.A., and Cabrera, C.R. (2019). Silver-palladium electrodeposition on unsupported vulcan XC-72R for oxygen reduction reaction in alkaline media. ACS Appl. Energy Mater. *2*, 4664–4673.

Wang, J., Chen, F., Jin, Y., and Lei, Y. (2018a). Dilute Au-containing Ag nanosponges as a highly active and durable electrocatalyst for oxygen reduction and alcohol oxidation reactions. ACS Appl. Mater. Interfaces *10*, 6276–6287.

Wang, Y., He, Q., Guo, J., Wang, J., Luo, Z., Shen, T.D., Ding, K., Khasanov, A., Wei, S., and Guo, Z. (2015). Ultrafine FePd nanoalloys decorated multiwalled carbon nanotubes toward enhanced ethanol oxidation reaction. ACS Appl. Mater. Interfaces *7*, 23920–23931.

Wang, X., He, Q., Song, L., Jaroniec, M., Zheng, Y., and Qiao, S.Z. (2019a). Breaking the volcano-plot limits for Pt-based electrocatalysts by selective tuning adsorption of multiple intermediates. J. Mater. Chem. A *7*, 13635–13640.

Wang, X., Li, Z., Qu, Y., Yuan, T., Wang, W., Wu, Y., and Li, Y. (2019b). Review of metal catalysts for oxygen reduction reaction: from nanoscale engineering to atomic design. Chem *5*, 1486–1511.

Wang, H., Wang, C., Liu, L., Qu, T., Wang, D., and Kang, Z. (2018b). Synthesis of Co-Fe-Pd nanoparticles via ultrasonic irradiation and their electro-catalytic activity for oxygen reduction reaction. Appl. Catal. A Gen. *560*, 103–110.

Wang, Y.J., Wilkinson, D.P., and Zhang, J. (2011). Noncarbon support materials for polymer electrolyte membrane fuel cell electrocatalysts. Chem. Rev. *111*, 7625–7651.

Wang, Y., Zhu, Z., Xu, K., Guo, W., Yu, T., He, M., Wei, W., and Yang, T. (2021). Palladium nanobelts with expanded lattice spacing for electrochemical oxygen reduction in alkaline media. ACS Appl. Nano Mater. *4*, 2118–2125.

Xie, S., Choi, S.-I., Lu, N., Roling, L.T., Herron, J.A., Zhang, L., Park, J., Wang, J., Kim, M.J., Xie, Z.X., et al. (2014). Atomic layer-by-layer deposition of Pt on Pd nanocubes for catalysts with enhanced activity and durability toward oxygen reduction. Nano Lett. *14*, 3570–3576.

Xie, Y., Li, C., Castillo, E., Fang, J., and Dimitrov, N. (2021). Nanoporous Pd-Cu thin films as highly active and durable catalysts for oxygen reduction in alkaline media. Electrochim. Acta *385*, 138306.

Xu, C., Liu, Y., Hao, Q., and Duan, H. (2013). Nanoporous PdNi alloys as highly active and methanoltolerantelectrocatalysts towards oxygen reduction reaction. J. Mater. Chem. A *1*, 13542–13548.

Xie, S., Lu, N., Xie, Z., Wang, J., Kim, M.J., and Xia, Y. (2012). Synthesis of Pd-Rh core-frame concave nanocubes and their conversion to Rh cubic nanoframes by selective etching of the

Pd cores. Angew. Chem. Int. Ed. *51*, 10266–10270.

Yang, G., Chen, D., Lv, P., Kong, X., Sun, Y., Wang, Z., Yuan, Z., Liu, H., and Yang, J. (2016). Core-shell Au-Pd nanoparticles as cathode catalysts for microbial fuel cell applications. Sci. Rep. *6*, 35252.

Yang, Y., Xiao, W., Feng, X., Xiong, Y., Gong, M., Shen, T., Lu, Y., Abruña, H.D., and Wang, D.

(2019). Golden palladium zinc ordered intermetallics as oxygen reduction electrocatalysts. ACS Nano *13*, 5968–5974.

Ye, W., Chen, S., Lin, Y., Yang, L., Chen, S., Zheng, X., Qi, Z., Wang, C., Long, R., Chen, M., et al. (2019). Precisely tuning the number of Fe atoms in clusters on N-doped carbon toward acidic oxygen reduction reaction. Chem *5*, 2865–2878.

STAR★METHODS

KEY RESOURCES TABLE

REAGENT or RESOURCE	SOURCE	IDENTIFIER
Chemicals, peptides, and recombinant proteins		
Palladium(II) acetylacetonate	Aladdin Co., Ltd	CAS: 14,024-61-4
Gold chloride trihydrate	Sinopharm Chemical Reagent	CAS: 16961-25-4
Nickel(II) acetylacetonate	J&K Scientific	CAS: 3264-82-2
Oleylamine	J&K Scientific	CAS: 112-90-3
Nafion117 solution	Sigma-Aldrich Co., Ltd	CAS: 31175-20-9
Ethanol	Beijing Chemical Works	CAS: 64-17-5
Methanol	Beijing Chemical Works	CAS: 67-56-1
n-hexane	Beijing Chemical Works	CAS: 110-54-3
Pd/C catalyst (20 wt% Pd loading)	Alfa Aesar Co., Ltd	Stock No.: 38308
Pt/C catalyst (20 wt% Pt loading)	Johnson Matthey	Stock No.: Hispec3000

RESOURCE AVAILABILITY

Lead contact

Further information and requests for resources and materials should be directed to and will be fulfilled by the Lead Contact, Jun Yang (jyang@ipe.ac.cn).

Materials availability

This study did not generate new unique reagents. All chemicals were obtained from commercial resources and used as received.

Data and code availability

Data reported in this paper will be shared by the lead contact upon request.

No new code was generated during the course of this study.

Any additional information required to reanalyze the data reported in this paper is available from the lead contact upon request.

METHODS DETAILS

Synthesis of core-shell Au@NiPd nanoparticles

For the synthesis of core-shell Au@NiPd nanoparticles with sub-nano NiPd alloy shells, an Au-catalyzed strategy we developed before was employed for synthesizing core-shell Au@Ni nanoparticles (Chen et al., 2016), which serve as sacrificial templates in subsequent replacement reaction with Pd^{2+} precursors. In detail, 0.1 mmol of $HAuCl_4 \cdot 4H_2O$ was add to 10 mL of oleylamine in a three-necked flask. The mixture was ultra-sonicated for 1 min, and then heated to 150°C under vigorous stirring for the formation of Au seeds. After 2 h, the temperature of the reaction system was lowered to 120°C, and 0.1 mmol of $Ni(acac)_2$ was added, followed by keeping the temperature at 120°C for 2 h for fulfilling the reduction of Ni^{2+} ions under the Au catalysis. It is noteworthy that without Au assistance, the reduction of Ni^{2+} ions in oleylamine at 120°C is not possible. As a result of Au catalysis, the Ni atoms continuously grow on the Au core and form a shell with thickness of up to three atomic layers. Then, different amount of $Pd(acac)_2$ (0.00625, 0.0125 and 0.025 mmol) was swiftly introduced, and the temperature was kept 3 more hours for completing the galvanic replacement reaction between the thin Ni shell and Pd^{2+} ions, which converts the pure Ni shells into NiPd alloy shells. Afterward, the final core-shell Au@NiPd products were firstly precipitated with methanol, washed twice with methanol, and collected by centrifugation at 8000 rpm for 3 min. Finally, the as-prepared core-shell nanostructures were re-dispersed in 10 mL of n-hexane, denoted as core-shell $Au@Ni_xPd_y$

nanoparticles, in which the *x* and *y* indicating the corresponding Ni/Pd atomic ratio in alloy shells were determined by inductively coupled plasma atomic emission spectroscopy (ICP-AES).

Synthesis of core-shell Au@Pd nanoparticles

Core-shell Au@Pd nanoparticles served as counterparts of core-shell Au@NiPd nanoparticles were also synthesized based on the Au catalysis (Chen et al., 2016). Analogously, after synthesis of Au seeds, the temperature of the reaction system was decreased to 100°C, followed by introduction of 0.1 mmol of Pd(acac)$_2$ precursors. Then after 2 h, the core-shell Au@Pd nanoparticles were formed, precipitated, washed, collected and re-dispersed in 10 mL of n-hexane.

Particle characterizations

The images of transmission electron microscopy (TEM) and high-resolution TEM (HRTEM) were taken using a JEOL JEM-2010F electron microscope operated at 200 kV. High-angle annular dark-field scanning TEM imaging (HAADF-STEM) was performed on an aberration-corrected JEM-ARM 200F operated at 300 kV, which provides a nominal image resolution of 0.07 nm. An energy dispersive X-ray spectroscopy (EDX) analyzer attached to the aberration-corrected JEM-ARM 200F operated in the STEM mode was used to analyze the element distributions of the obtained core-shell nanostructures. Powder X-ray diffraction (XRD) patterns of the samples were recorded by a Bruker D8 diffractometer using Cu K$_\alpha$ radiation (λ = 0.154056 nm), and the X-ray photoelectron spectra (XPS) were collected using a Thermo Scientific K-Alpha XPS spectrometer. The ICP-AES test was conducted on Thermo Scientific 6300 to determine the accurate content of the corresponding component in as-prepared core-shell samples.

Electrochemical measurements

For the electrochemical measurements, core-shell Au@NiPd nanoparticles and their core-shell Au@Pd counterparts were loaded on the active carbon substrate. The calculated amounts of carbon powder were added to the hexane solution of core-shell nanoparticles. After stirring for 6 h, the carbon supported samples were collected by centrifugation and dried at room temperature in a vacuum. The accurate contents of the Pd loaded on carbon substrates were determined by ICP-AES.

Electrochemical measurements were conducted on a standard three-electrode cell that was connected to a Bio-logic VMP3 potentiostat. A leak-free Ag/AgCl electrode and a platinum mesh (1 × 1 cm^2) attached to a platinum wire were used as the reference and counter electrode, respectively. All potentials were converted to values with reference to RHE.

The working electrode was prepared as follows: 5 mg of the carbon-supported nanoparticles was ultrasonically dispersed in 1 mL of ethanol containing 0.05 mL of Nafion solution. Subsequently, 5 μL of the ink was dropped onto the 5-mm glassy carbon disk electrode, which was then dried in a warm air stream at 70°C for 1 h. The electrochemically active surface areas (ECSAs) of these Pd-based nanostructures were determined based on the electrochemical CO stripping curves, and were calculated using an equation in term of ECSA = Q/420G, where Q is the charge of the desorption of CO in microcoulomb (μC), which is calculated by dividing the scan rate (0.05 V s^{-1}) with the integral area of the stripping peak, G represents the mass loading of Pd (μg) on the electrode determined by ICP-AES, and 420 is the theoretical charge (μC cm^{-2}) for stripping a monolayer of CO from the surface of catalysts.

The linear sweep voltammetry (LSV) curves of core-shell Au@NiPd nanoparticles, core-shell Au@Pd nanoparticles, commercial Pd/C and Pt/C catalysts for ORR at room temperature were obtained by rotating disk electrode (RDE) tests, which were carried out in an O$_2$-saturated 0.1 M KOH solution with a scan rate of 10 mV s^{-1} at different rotation rates. The RDE tests of core-shell Au@NiPd nanoparticles and commercial Pt/C catalysts in the acidic medium were performed in 0.1 M HClO$_4$ solution with a scan rate of 10 mV s^{-1} at a rotating speed of 1600 rpm. Rotating Disk Ring Electrode (RRDE) tests also were performed in the same condition, and the ring electrode was held at 1.4 V to collect the peroxide generated at the disk electrode. The yield of the peroxide was calculated by the followed formula:

$$H_2O_2\% = \frac{2I_R/N}{I_D + I_R/N} \times 100\%$$

where I$_D$ and I$_R$ are the absolute value of the disk and the ring current and N (calculated value is 0.15) is the RRDE collection efficiency. Electrochemical impedance spectroscopy (EIS) was measured in the frequency

range from 10^6 to 0.01 Hz. The long-term durability tests were performed by continuously sweeping potential cycles in the potential range of 0.6–1.0 V vs. RHE with an accelerated sweep rate of 100 mV s^{-1} in an O_2-saturated 0.1 M KOH solution at room temperature. After the durability tests, the catalysts on the RDE were re-dispersed ultrasonically into ethanol for charactering their morphology and composition.

Calculation details

DFT calculations were performed using the Vienna ab-initio simulation package (VASP) (Kresse and Furthmüller, 1996a, 1996b). The projector-augmented wave (PAW) method (Perdew et al., 1996) was used to describe the ionic cores and take valence electrons into account using a plane wave basis set with a kinetic energy cutoff of 450 eV. The generalized gradient approximation (GGA) with the Perdew-Burke-Ernzerhof (PBE) exchange-correlation functional (Kresse and Joubert, 1999) was used in our calculations. Geometry optimizations were performed with the force convergency smaller than 0.03 eV Å^{-1}. The Brillouin zone is sampled with 3 × 3 × 1 Monkhorst mesh (Monkhorst and Pack, 1976). The free energy on surface was calculated using the equation in form of $\Delta G = E$ (DFT) $+ \Delta E$ (ZPE) $- T\Delta S$, Where E (DFT) is the total energy for the adsorption OOH*, OH* and O*, ΔE (ZPE) is the zero-point energy change, and ΔS is the entropy change.